ORIGINAL ARTICLE

Evolution of microstructure and mechanical characteristics of (CrFeNiCu)$_{100-x}$Ti$_x$ high-entropy alloys

Yusupov Dilshodbek, Sung Hwang Hong* , **Muhammad Aoun Abbas, Gyeol Chan Kang, Hae Jin Park, Elyorjon Jumaev, Wei-Min Wang, Ki Buem Kim***

Abstract (CrFeNiCu)$_{100-x}$Ti$_x$ (x = 0, 3, 5, 7 and 10; at%) high-entropy alloys have been designed by the consideration of the thermophysical relationship between Ti and other principal elements to investigate the influence of Ti on the microstructural evolution and mechanical properties of (CrFeNiCu)$_{100-x}$Ti$_x$ high-entropy alloys. The addition of Ti content in HEAs leads to a change in phase formation from dual-phase (FCC1 and FCC2, FCC: face-centered cubic) to the mixture of FCC1, FCC2 phases, and an additional body-centered cubic (BCC) phase. The yield strength and Vickers hardness of the alloys are enhanced from 291 to 1511 MPa and HV 134 to HV 531, respectively, which depends strongly on the volume fraction of BCC phase. On the one hand, the plasticity of the alloys reduces from 45.00% to 24.09%, but it could be considered reasonable plasticity. These results revealed that the addition of a minor alloying element in high-entropy alloys with consideration of thermophysical parameters led to the formation of a multiple solid solution structure with excellent mechanical properties.

Keywords High-entropy alloy (HEA); Microstructure; Mechanical properties; Theoretical parameters

Yusupov Dilshodbek and Sung Hwan Hong have contributed equally to this work.

Y. Dilshodbek, S. H. Hong*, M. A. Abbas,
G. C. Kang, H. J. Park, K. B. Kim*
Department of Nanotechnology and Advanced Materials Engineering, Sejong University, Seoul 05006, Republic of Korea
e-mail: shhong@sejong.ac.kr

K. B. Kim
e-mail: kbkim@sejong.ac.kr

E. Jumaev
Almalyk Mountain Mining Complex(MMC), Almalyk City 110100, Republic of Uzbekistan

W.-M. Wang
School of Materials Science and Engineering, Shandong University, Jinan 250100, China

K. B. Kim
Department of Chemical Engineering, New Uzbekistan University, Tashkent 100007, Republic of Uzbekistan

1 Introduction

High-entropy alloys (HEAs) have attracted considerable attention during the last decade by considering the entropy of materials to develop high-performing metallic materials [1–3]. HEAs include four or more principal elements with concentrations in the range of 5 at%–35 at% in equal or near-equal proportions compared with conventional alloys with one or two principal elements [1, 3–6]. The high value of mixing entropy in HEAs induces the kinetically slow atomic diffusivity, which promotes the development of simple solid solution phases such as body-centered cubic (BCC), face-centered cubic (FCC), and mixture solid solution (BCC + FCC). It also strongly suppresses the formation and precipitation of additional stable phases at room temperature [7]. From the simple solid solution structure with high solubility, the HEAs have presented excellent mechanical and physical characteristics, including high strength, large ductility [8, 9], high hardness [10, 11], valuable oxidation [12, 13], and corrosion resistance due to severe lattice distortion and cocktail effects.

New parameters and criteria for phase prediction have been suggested to design reasonable alloy compositions of HEAs using mixing enthalpy (ΔH_{mix}) [14], mixing entropy

(ΔS_{mix}) [1, 4, 15], atomic size difference (δ) [16], and valence electron concentration (VEC) [6, 17]. The formation of a solid solution phase is particularly achievable when the parameters conform to $\delta \leq 6.6$ and by $\Omega \geq 1.1$, where Ω is the scale ratio of ΔS_{mix} to ΔH_{mix} [14, 16, 18]. Furthermore, competition between the formation of FCC and BCC phases can be predicted by modulating the VEC value of alloys [6, 17]. Nevertheless, this criterion has been not always useful to predict the phase formation in HEA, considering some aspects of alloy design. Further experimental explorations are required to recognize the suggested criterion from previous reports. The VEC values of HEAs decrease from 8.8 to 8.352, indicating a stable FCC region in (CoCrCuFeNi)$_{100-x}$Mo$_x$ ($x = 0 - 16$ at%) HEAs [19]. However, the constituent phases of HEAs change from single FCC phase to FCC + BCC phases even though the VEC values of HEAs are higher than 8. There have been many approaches for development of HEAs, such as CoCrFeNi, FeCoNiCrMn, FeCoNiCrMo, FeCoNiCrAl, and CoCrFeMnNiV [19–21], that help understand the influence of minor elements on the structural changes and mechanical behavior. As Co, Cr, Fe, and Ni are the major constituents of the HEA, it is expected that the crystal structure of HEAs will be FCC, BCC, or a combination of both [4, 15, 22]. The addition of Cu in an HEA usually leads to

the formation of another Cu-rich FCC phase in the interdendrite region [23, 24]. The impact of minor elements such as Al, V, Ti, and Mo can be observed in unexpected structural features [20, 25, 26]. These previous studies suggest that the phase formation, microstructure, and mechanical characteristics of HEAs can be altered with the addition of minor elements.

In this work, we designed (CrFeNiCu)$_{100-x}$Ti$_x$ HEAs with $x = 0, 3, 5, 7,$ and 10 at% to investigate the influence of Ti addition on the microstructure and mechanical properties of the CrFeNiCu HEA system. Ti was selected as a minor alloying element considering the thermophysical parameters (Fig. 1 and Table 1). ΔH_{mix}, ΔS_{mix}, T_m, δ, and VEC of the (CrFeNiCu)$_{100-x}$Ti$_x$ HEAs were estimated in order to understand the relation between phase formation and thermophysical parameters. Furthermore, the microstructural evolution, mechanical properties, and deformation behavior of HEAs were systematically investigated.

2 Experimental

(CrFeNiCu)$_{100-x}$Ti$_x$ HEA ingots were prepared by using the vacuum-arc-melting method with high purity Cr, Fe, Ni, Cu and Ti (> 99.95 wt% elemental purity). To ensure chemical homogeneity of alloys, the ingots were re-melted at least five times on a water-cooled copper hearth in a Ti-getter under high purity argon atmosphere. The as-cast rod-type samples were fabricated using the suction casting method into a water-chilled cylindrical copper mold with 50 mm in length and 3 mm in diameter. The phase identification of the as-cast samples was conducted by using X-ray diffraction (XRD, Empyrean, PANalytical, Malvern, United Kingdom) with Cu Kα radiation ($\gamma = 0.15406$ nm) in the 2θ scan range of $20° - 80°$ with step size of 0.026°, time per step of 50 s, a voltage of 30 kV, and current of 40 mA. The microstructural observation and chemical analysis of the as-cast samples were examined using field emission scanning electron microscopy (FESEM, JEOL JSM-6390; JEOL, Tokyo, Japan) equipped with energy-dispersive X-ray (EDX, HITACHI SU-8010, Hitachi, Tokyo, Japan). Transmission electron microscopy (TEM, Tecnai-F20 G2, FEI Company, Hillsboro, USA) equipped with energy dispersive spectrometry (EDS, BRUKER QUANTAX 400, Bruker, MA, USA) was conducted to analyze the detailed microstructure and elemental distribution under an accelerating voltage of 200 kV. Thin specimens for TEM analysis were prepared by using ion milling under liquid-nitrogen cooling. Mechanical properties of the as-cast samples were examined by compression test at a strain rate of 1×10^{-3} s^{-1} using a universal testing machine (UTM, Z050, Zwick/Roell corporation, Ulm, Germany), and the cylindrical samples were prepared with aspect ratio of 2:1 (Φ3 mm $\times$ 6 mm). The hardness of
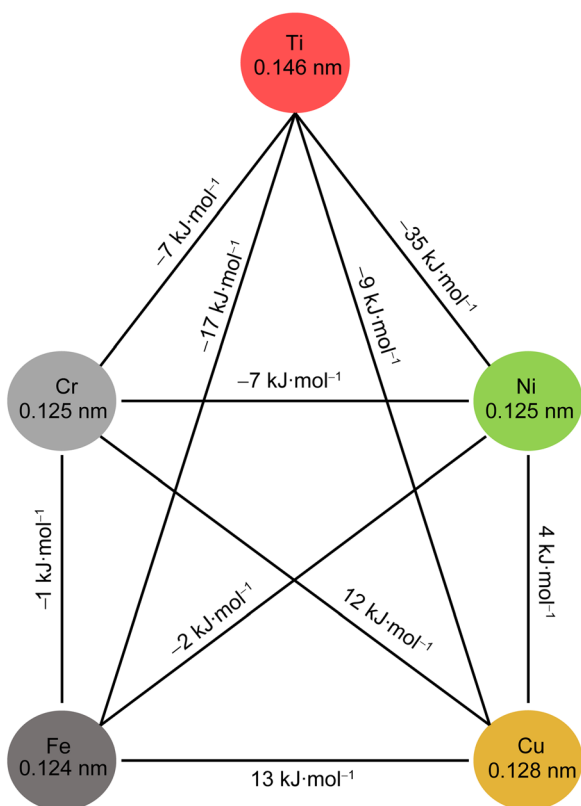
Fig. 1 Mixing enthalpy (ΔH_{mix}) between constituent elements and atomic radius

Table 1 ΔS_{mix}, ΔH_{mix}, δ, VEC and Ω values of as-cast $(CrFeNiCu)_{100-x}Ti_x$

Alloys	ΔS_{mix} / (J·K^{-1}·mol^{-1})	ΔH_{mix} / (kJ·mol^{-1})	δ / %	VEC	Ω
CrFeNiCu	11.520	4.750	1.237	8.75	4.930
$(CrFeNiCu)_{97}Ti_3$	12.294	2.490	3.063	8.60	9.159
$(CrFeNiCu)_{95}Ti_5$	12.594	1.057	3.776	8.51	22.130
$(CrFeNiCu)_{93}Ti_7$	12.821	− 0.319	4.342	8.41	74.830
$(CrFeNiCu)_{90}Ti_{10}$	13.070	− 2.273	5.024	8.27	10.710

all as-cast samples was measured using the micro-Vickers hardness tester (HMV-G, Shimadzu corporation, Kyoto, Japan) with a load of 980.7 mN and a loading time of 10 s at room temperature. The hardness measurement of each as-cast sample was repeated more than 8 times. The average hardness values were calculated and presented in this work.

3 Results and discussion

3.1 Theoretical calculations

The thermophysical parameters have been considered a factor to predict the crystal structures of HEAs. Previous studies [1, 4, 6, 14–17] have reported the relationship between phases and thermophysical parameters: Ω, ΔS_{mix}, ΔH_{mix} and δ. Especially, Zhang et al. [27] and Guo and Liu [6] have studied the influence of ΔH_{mix} and ΔS_{mix} on phase formation of HEA, which are considered as important thermodynamic parameters. The following conditions must be met simultaneously to form simple solid solutions: -22 kJ·mol$^{-1} \leq \Delta H_{mix} \leq 7$ kJ·mol^{-1}, $\delta \leq 8.5$, and 11 kJ·mol$^{-1} \leq \Delta S_{mix} \leq 19.5$ kJ·mol^{-1} [3]. If ΔH_{mix} value is large positive, phase segregation achieves, whereas large negative ΔH_{mix} value leads to forming intermetallic compounds. ΔH_{mix} between constituent elements and atomic radius is summarized in Fig. 1. Cu has positive ΔH_{mix} values with Cr, Fe and Ni, indicating possibility of phase separation. Ti and Ni show a highest positive ΔH_{mix} value, which imply possibility on formation of intermetallic compound.

Thermophysical parameters are calculated to predict the crystal structure of $(CrFeNiCu)_{100-x}Ti_x$ using Eqs. (1–4).

$$\Omega = \frac{T_m \Delta S_{mix}}{|\Delta H_{mix}|} \tag{1}$$

$$T_m = \sum_{i=1}^{n} c_i (T_m)_i \tag{2}$$

$$\Delta S_{mix} = -R \sum_{i=0}^{n} c_i \ln c_i \tag{3}$$

$$\Delta H_{mix} = \sum_{i=1, i \neq j}^{n} \Omega_{ij} c_i c_j \tag{4}$$

where T_m is the melting temperature, n is the number of elements in an alloy system, c_i and c_j are the molar fraction of the ith and jth elements, respectively, R is the gas constant (8.314 J·K^{-1}·mol^{-1}), and $\Omega_{ij} = \Delta H_{mix}^{ij}$ where ΔH_{mix}^{ij} is the mixing enthalpy between the ith and jth elements. To calculate the ΔH_{mix} of $(CrFeNiCu)_{100-x}Ti_x$ HEAs, previous study on ΔH_{mix} of atomic pairs reported by Takeuchi and Inoue [14] was used. ΔS_{mix}, ΔH_{mix} and Ω values of $(CrFeNiCu)_{100-x}Ti_x$ HEAs are listed in Table 1.

δ is effective to predict the lattice distortion in the crystal structure using Eq. (5) [16, 27, 28]:

$$\delta_r = \sqrt{\sum_{i=1}^{n} c_i \left(1 - \frac{r_i}{\bar{r}}\right)^2} \tag{5}$$

The value of δ is calculated using c_i, and r_i is the atomic radius of each element shown in Table 1. The condition of $\Omega > 1.1$ and $\delta < 6.6$ are required to develop a simple solid solution structure [18]. Ω and δ values of $(CrFeNiCu)_{100-x}Ti_x$ HEAs are in a range of 4.93−74.83 and 1.237−5.024, respectively, with varying Ti content. Therefore, it can be expected that $(CrFeNiCu)_{100-x}Ti_x$ ($x = 3$, 5, 7 and 10; at%) HEAs consist of simple solid solution structure. Although the formation of a solid solution can be predicted by Ω and δ, the crystal structure of the solid solution phase cannot be determined. According to the study of Guo et al. [17], the phase stability of HEAs can be determined using VEC:

$$VEC = \sum c_i VEC_i \tag{6}$$

where VEC is the number of valence electrons per element. Based on previous works [6, 17], it can be concluded that (1) when VEC ≥ 8, FCC phase is stable, (2) when VEC ≤ 6.87, BCC phase is stable, and (3) a mixture of FCC and BCC phases was observed when $6.87 \leq$ VEC ≤ 8. The calculated VEC values of $(CrFeNiCu)_{100-x}Ti_x$ ($x = 0$, 3, 5, 7 and 10; at%) HEAs are in the range of 8.27–8.75 (Table 1), indicating the formation of FCC phase. Based on these investigations of thermophysical parameters of HEAs, it can be predicted that the $(CrFeNiCu)_{100-x}Ti_x$ ($x = 0$, 3, 5, 7, and 10 at%) HEAs can be formed as simple solid solutions.
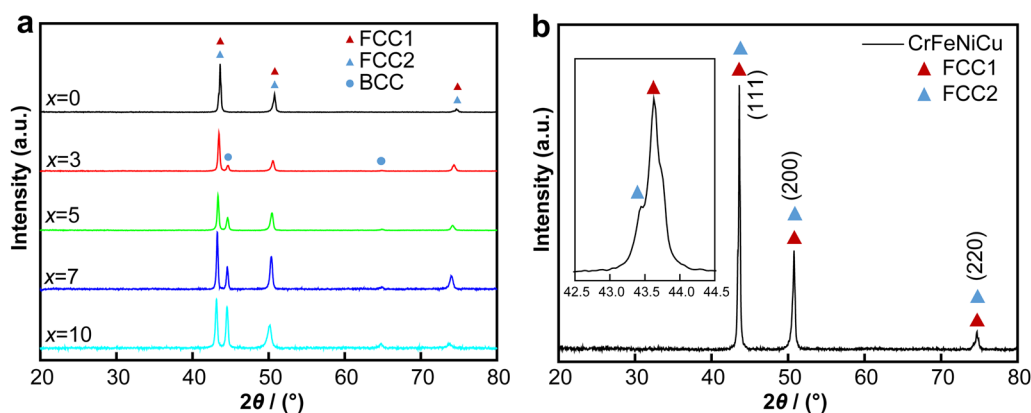
Fig. 2 **a** XRD patterns of as-cast $(CrFeNiCu)_{100-x}Ti_x$ ($x = 0, 3, 5, 7$ and 10; at%) HEAs; **b** XRD patterns of as-cast CrFeNiCu HEA and (inset) magnified (111) peaks of FCC1 and FCC2 phases

3.2 Microstructure and phase identification

The phase identification of the as-cast $(CrFeNiCu)_{100-x}Ti_x$ ($x = 0, 3, 5, 7,$ and 10 at%) HEAs was conducted by XRD analysis, as shown in Fig. 2. The sharp diffraction peaks corresponding to (111), (200), and (220) planes of the FCC phase are present in all the samples, as shown in Fig. 2a. Figure 2b shows two overlapped peaks with different intensities at 2θ range of $43.0°-44.5°$ (inset XRD trace in Fig. 2b), which correspond to the FCC phase, indicating a dual-FCC structure with a similar lattice constant. With Ti content increasing up to 10 at%, the peaks corresponding to the FCC phase are presented in all the samples, as shown in Fig. 2a. The BCC peaks corresponding to (110) and (200) planes at 2θ ranges of $44°-45°$ and $64°-65°$ present in the as-cast $(CrFeNiCu)_{97}Ti_3$ alloy. Thus, the addition of Ti content to CrFeNiCu HEA induces the formation of the BCC phase. The peaks of BCC phase increase gradually by adding Ti content up to 10 at%, which indicates that the volume fraction of the BCC phase gradually increases with Ti content increasing while maintaining FCC1 and FCC2 phases. The peaks of FCC1, FCC2, and BCC phases shift slightly to a lower 2θ values, indicating an increase in the lattice constant of phases due to the addition of Ti with a larger atomic radius than that of other elements (Fig. 1). The atomic radius of Ti (0.147 nm) is larger than those of other constitutional elements Cr (0.128 nm), Fe (0.126 nm), Ni (0.124 nm), and Cu (0.128 nm) [29]. The lattice constant of FCC and BCC phases is calculated from XRD results to identify the change of lattice constant of each phase in HEAs. The lattice constant of the FCC phase is 1.933 nm in CrFeNiCu HEA. The lattice constant of FCC and BCC phases increases from 1.993 to 1.951 nm and from 1.549 to 1.582 nm, respectively, after the addition of Ti. Based on phase formation of HEAs as identified in XRD result, it can be concluded that the addition of a small amount of Ti content to CrFeNiCu HEA stabilizes and increases the compatibility of BCC phase compared with

both FCC phases during solidification. The VEC values of $(CrFeNiCu)_{100-x}Ti_x$ HEAs are higher than 8, favoring the formation of FCC phase [6]. Nevertheless, the addition of Ti content initiates the the formation of the multiple solid solutions comprising FCC1, FCC2 and BCC phases, which contradicts VEC rules from previous report [6]. This result suggests that other thermophysical parameters may play an important role to modulate phase stability of HEAs. In previous studies, the exceptions of VEC rules have been often reported: (i) Wu et al. [30] reported formation of FCC and BCC phases in $Cr_xFeNiCu$ HEAs with higher VEC than 8; (ii) Guo et al. [17] reported formation of sole FCC phase in $Al_xCoCrCu_{0.5}FeNi$ HEAs when VEC value is in the range of $6.87-8.0$, favoring mixture of FCC and BCC phases. These exceptions are considered as deviation from the VEC rules. Therefore, detailed investigations of the microstructure and chemical composition of HEAs were conducted to understand the influence of Ti on the microstructural evolution of $(CrFeNiCu)_{100-x}Ti_x$ HEAs.

The microstructure of as-cast $(CrFeNiCu)_{100-x}Ti_x$ HEAs was investigated via SEM back-scattered electron (BSE) micrograph, as shown in Fig. 3. The as-cast CrFeNiCu HEA shows a typical dual-phase structure of dendrite and interdendrite, as shown in Fig. 3a. XRD analysis (Fig. 2) also shows both dendrite and intedendrite phases identified as FCC1 and FCC2 phases for this sample. The spectra of $(CrFeNiCu)_{100-x}Ti_x$ HEAs with $x = 3, 5, 7,$ and 10 at% shown in Fig. 3b−e reveal three different phases with dark, gray, and bright contrast, denoted as 1, 2 and 3, respectively. The small dark phase is newly formed in $(CrFeNiCu)_{97}Ti_3$ HEA and is surrounded by the gray phase forming a shell-like structure. The bright phase (marked by 3) is still located in the interdendrite region. The morphology of the dendrite region changes to a spherical shape. The phase fraction of the dark phase gradually increases with increasing Ti concentration up to 10 at%. However, both gray and bright phases continue to form in the dendrite and interdendrite regions. The
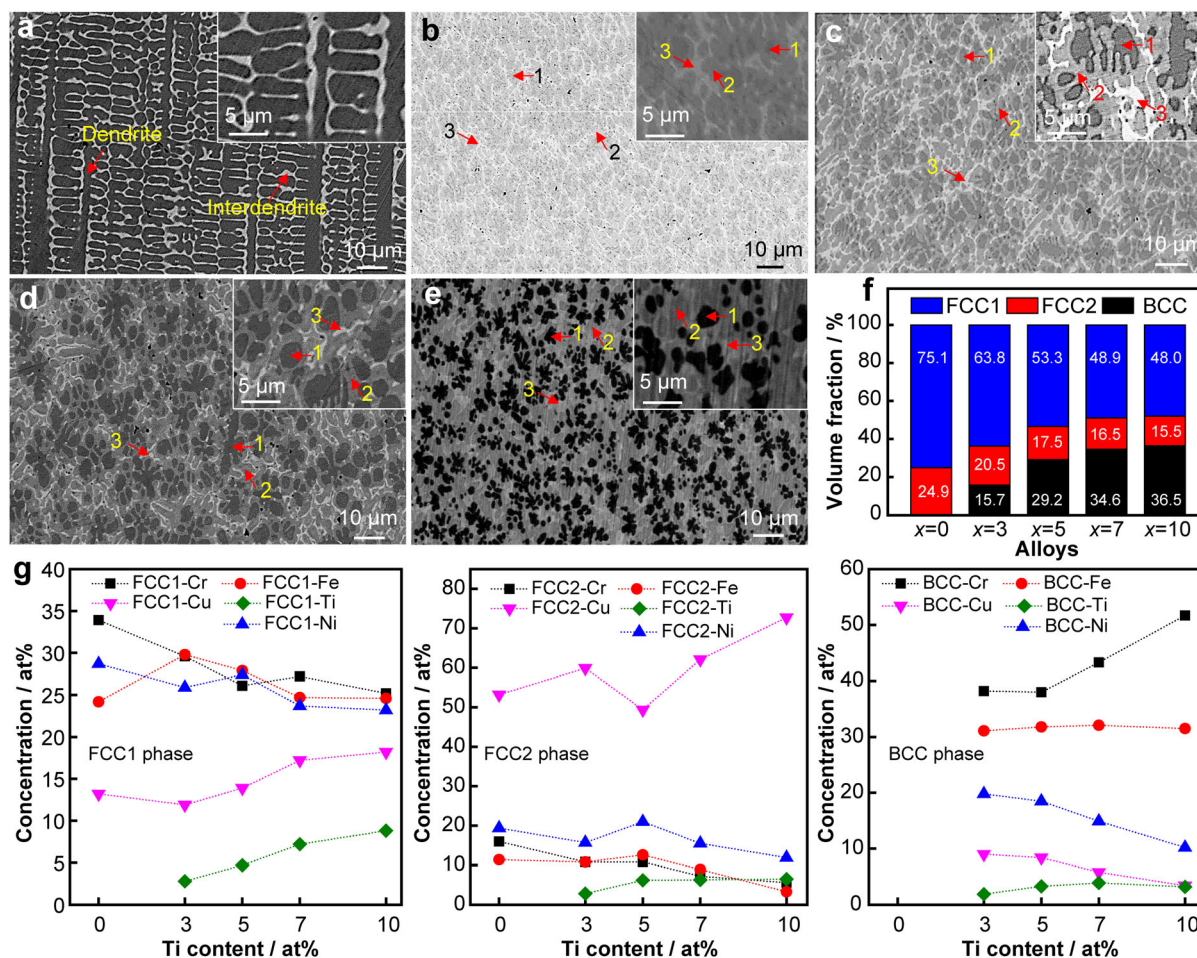
Fig. 3 SEM-BSE images of as-cast $(CrFeNiCu)_{100-x}Ti_x$ HEAs: **a** $x = 0$, **b** $x = 3$, **c** $x = 5$, **d** $x = 7$, and **e** $x = 10$, where red arrows marked by 1, 2 and 3 in **b**–**d** indicate BCC, FCC1 and FCC2 phases, respectively; **f** volume fraction of FCC1, FCC2 and BCC phases depending on Ti content; **g** chemical evolution in FCC1, FCC2 and BCC phases depending on Ti content

morphology of the dendrite region becomes more spherical with increasing Ti content, but the shell-like structure of dark and gray phases disappears with dark phase randomly formed in the whole area. Based on these results with XRD analysis in Fig. 2, the dark, gray, and bright phases formed in the as-cast HEAs containing Ti content are identified as BCC, FCC1, and FCC2 phases, respectively. The volume fraction of constituent phases in the HEAs is measured by the pixel analysis using Photoshop CS6 as illustrated in Fig. 3f. The volume fraction of the BCC phase gradually increases with an increase in Ti content. The volume fractions of FCC1 and FCC2 phases are 75.1% and 24.9% for as-cast CrFeNiCu HEA, respectively, and decrease to 48.0% and 15.5%, respectively, on increasing Ti content up to 10 at%. Meanwhile, the volume fraction of BCC phase gradually increases to 36.5% with Ti content increasing up to 10 at%. The volume ratios of FCC1 and FCC2 phases have similar values ($V_{FCC2}/V_{FCC1} \approx 0.32$) in all alloys. Thus, a minor addition of Ti content to CrFeNiCu HEA induces the formation of BCC phase, indicating that the volume fraction of BCC phase strongly depends on the

amount of Ti. This result well coincides with previous reports on $AlCoCrFeNiTi_x$ and $CrFeNiAl_xTi_y$ HEAs [26, 31].

The chemical composition of constituent phases in $(CrFeNiCu)_{100-x}Ti_x$ HEAs was examined by FESEM EDS analysis as illustrated in Fig. 3g and listed in Table 2. The dendrite and interdendrite phases in as-cast CrFeNiCu HEA are considered as CrFeNi-rich FCC1 and Cu-rich FCC2 phases, respectively. The segregation of Cu in the interdendrite region of as-cast CrFeNiCu HEA results from a positive ΔH_{mix} between Cu and other elements (Fig. 1) [30, 32–34]. The distribution of elements was separated into three phases after adding Ti content to form $(CrFeNiCu)_{100-x}Ti_x$ HEAs, as shown in Fig. 3g. (i) FCC1 phase shows a slight decrease in Cr, Fe and Ni with an increase in Cu and Ti, (ii) the FCC2 phase also exhibits an increase in Cu with an increased Ti content, and (iii) the BCC phase, enriched with Cr and Fe, shows that Cr significantly increases with increasing Ti content. By contrast, Fe in the BCC phase remains almost constant, whereas Ni and Cu gradually decrease. This result suggests that an increase in

Table 2 Chemical composition of constituent phases in as-cast $(CrFeNiCu)_{100-x}Ti_x$ HEAs

Alloys	Phases	Content / at%				
		Cr	Fe	Ni	Cu	Ti
CrFeNiCu	FCC1	33.9	24.2	28.7	13.2	–
	FCC2	16.0	11.4	19.4	53.2	–
$(CrFeNiCu)_{97}Ti_3$	BCC	38.2	31.1	19.8	9.0	1.9
	FCC1	29.6	29.8	25.9	11.9	2.8
	FCC2	10.8	10.8	15.7	59.9	2.8
$(CrFeNiCu)_{95}Ti_5$	BCC	38.0	31.8	18.5	8.4	3.3
	FCC1	26.1	27.9	27.4	13.9	4.7
	FCC2	10.8	12.6	21.0	49.4	6.2
$(CrFeNiCu)_{93}Ti_7$	BCC	43.3	32.1	14.9	5.8	3.9
	FCC1	27.2	24.7	23.7	17.2	7.2
	FCC2	7.2	8.9	15.5	62.1	6.3
$(CrFeNiCu)_{90}Ti_{10}$	BCC	51.7	31.5	10.2	3.4	3.2
	FCC1	25.2	24.6	23.2	18.2	8.8
	FCC2	5.6	3.3	11.9	72.7	6.5

Ti content in $(CrFeNiCu)_{100-x}Ti_x$ HEAs leads to forming Cr(Fe)-enriched BCC phase as a primary phase due to the high melting temperature of Cr and relatively low negative ΔH_{mix} (-7 kJ·mol^{-1}) between Ti and Cr in comparison with those of Ti and other elements. The remaining liquid phase after the primary reaction of the Ti-containing HEAs has a relatively higher Cu content compared to the CrFeNiCu HEA devoid of Ti. Therefore, an increase in the volume fraction of the Cr(Fe)-enriched BCC phase with an increase in Ti content induces the formation of FCC1 and FCC1 phases containing a higher amount of Cu.

Based on the results of XRD and SEM, it was difficult to identify the exact crystal structure of $(CrFeNiCu)_{100-x}Ti_x$ HEAs because of the complexation of FCC1 and FCC2 peaks in XRD patterns. $(CrFeNiCu)_{95}Ti_5$ HEA consisting of FCC1, FCC2, and BCC phases was further analyzed to identify the detailed structural features. Figure 4a illustrates a TEM high-angle annular dark field (HAADF) image of the alloy with three different phases: BCC (dark), FCC1 (gray), and FCC2 (bright) regions. The phases are marked separately by yellow dashed lines. Selected area electron diffraction (SAED) patterns in Fig. 4b, c of FCC1 and FCC2 regions correspond to the [001] zone axis of the FCC structure and exhibit similar d-spacing of the (200) plane: 0.186 and 0.179 nm for FCC1 and FFC2 phases, respectively. SAED pattern of the BCC region in Fig. 4d also confirms the [001] zone axis of BCC structure, and d-spacing (110) plane is 0.197 nm. The lattice parameters of the FCC1, FCC2, and BCC phases calculated from SAED patterns are 0.322,
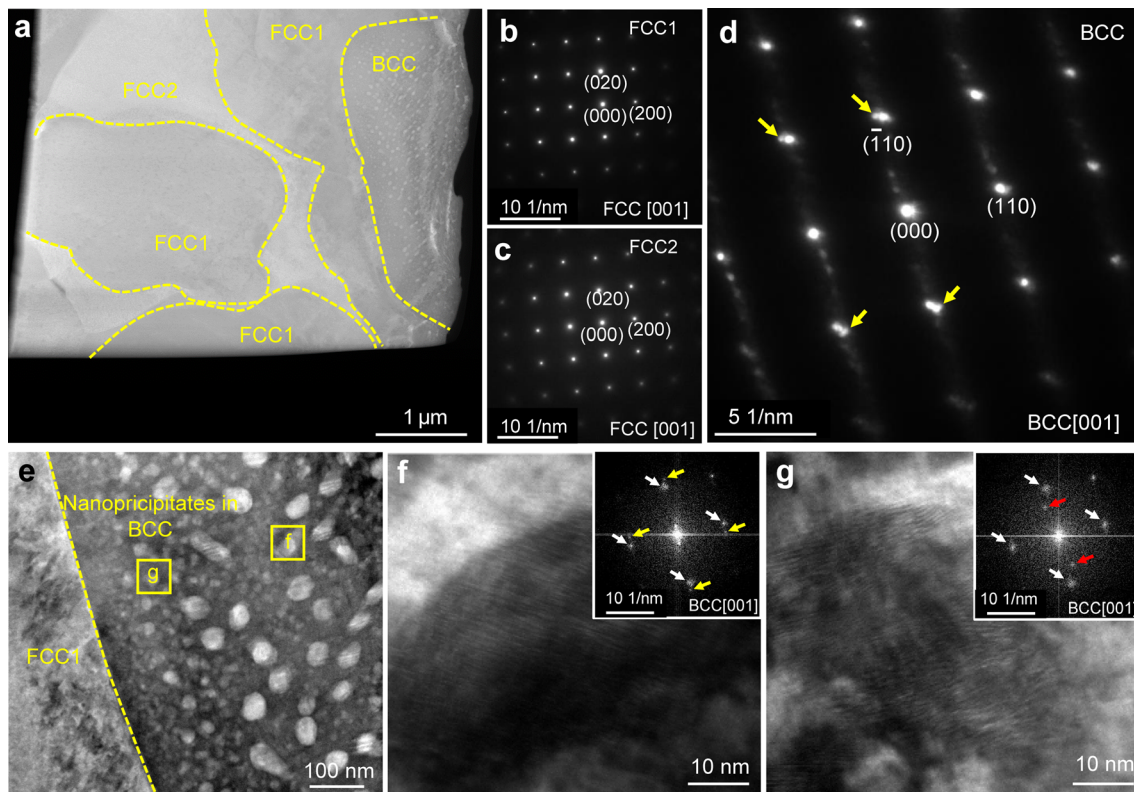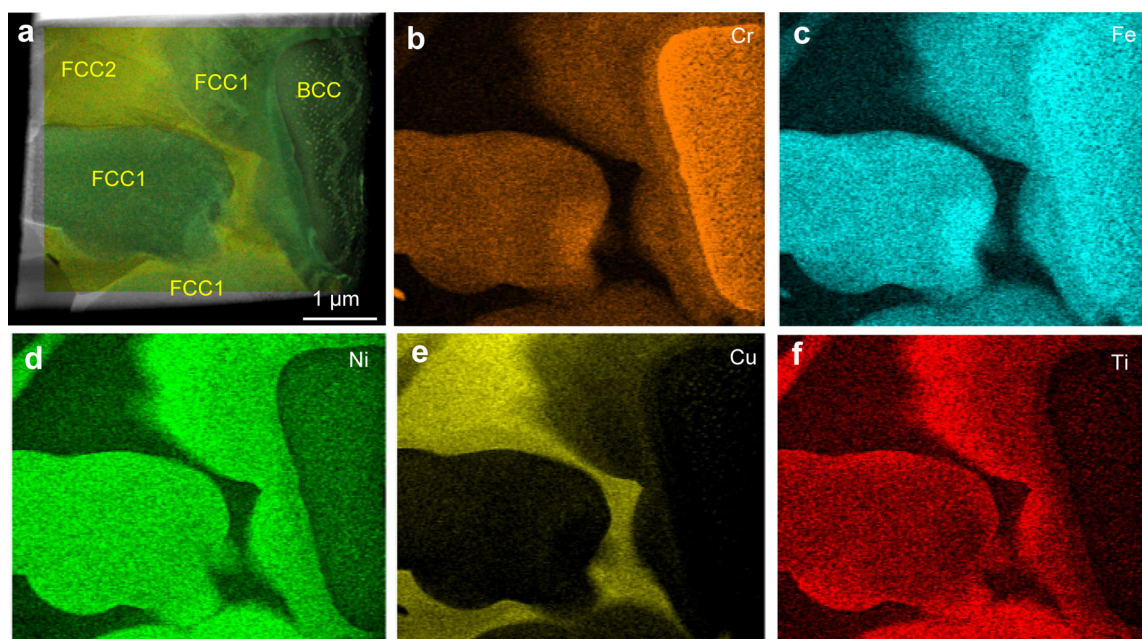

Fig. 4 **a** TEM-HAADF image of as-cast $(CrFeNiCu)_{95}Ti_5$ HEA; **b–d** SAED patterns corresponding to FCC1, FCC2, and BCC region, respectively; **e** higher-magnified TEM-HAADF image of BCC region in **a**; **f**, **g** HRTEM images corresponding to regions in **e** with inset being FFTs

0.325, and 0.279 nm, respectively. Interestingly, the bright nanoprecipitates with size of 10−60 nm are found in BCC region in Fig. 4a. The SAED pattern in Fig. 4d also reveals weak satellites (marked by yellow arrows) corresponding to nanoprecipitates around diffraction spotty of the BCC phase. A higher-magnified TEM-HAADF image of BCC region (Fig. 4e) clarifies the formation of bimodal-shaped bright nanoprecipitates (marked by yellow squares) embedded in the BCC phase. High resolution (HR) TEM images in Fig. 4f, g display a relatively large nanoprecipitate of 'f' region and the small nanoprecipitete of 'g' region in Fig. 4e. The fast Fourier transform (FFT) patterns obtained from HRTEM images in the insets reveal that: (i) diffraction spots corresponding to [001] zone axis of FCC (mark by yellow arrows) and BCC (mark by white arrows) structures, as shown in Fig. 4f and (ii) diffraction spots of super lattice of $L1_2$ structure (marked by red arrows) near the diffraction spots of BCC (mark by white arrows), as shown in Fig. 4g. This result indicates that the nano-scale solute partitioning occurs in BCC phase during solidification, which forms two different nanoprecipitates with FCC and $L1_2$ structure. Ti, known as the strong $L1_2$ formers, is a favored choice for $L1_2$ formation [35]. Moreover, Cu element contributes on the stabilization and nucleation of the $L1_2$ phase [35, 36]. The $L1_2$ precipitate with BCC phase is also found in the Al_xCr-$CuFeNi_2$ and $Al_{0.5}Cr_{0.9}FeNi_{2.5}V_{0.2}$ HEAs [37, 38].

The elemental distributions in each phase of $(CrFeNiCu)_{95}Ti_5$ HEA are measured using TEM-EDS elemental maps. Figure 5a shows HAADF image obtained from the same area as the HAADF image in Fig. 4a. The corresponding EDS elemental maps of Cr, Fe, Ni, Cu and Ti are shown in Fig. 5b−f. Cr and Fe are concentrated mainly in BCC and FCC1 phases, whereas Ni and Ti are mainly distributed in FCC1 phase. Cu is strongly segregated in FCC2 phase of the interdenrite region. Regarding the TEM-EDS analysis, FCC1, FCC2 and BCC phases are identified as CrFeNi-rich, Cu-rich, and CrFe-rich phases, respectively. From the previous studies [39, 40], it is reported that the segregation of Ti in CrFeNi-enriched phase is caused by a large negative ΔH_{mix} value of Ti and Ni pairs compared to those of elements. Alternately, the high concentration of Cu in the interdendrite region results from the positive ΔH_{mix} value between Cu and Cr, Fe, and Ni, and the low melting temperature of Cu compared with those of other constituent elements [14, 41].

Figure 6 shows the TEM-EDS analysis of nanoprecipitates formed in BCC phase, as shown in Fig. 4e. HAADF image in Fig. 6a displays bimodal-shaped nanoprecipitates embedded in BCC phase, and the corresponding EDS elemental maps of Cr, Fe, Ni, Ti, and Cu are shown in Fig. 6b−f. The dark region of the BCC phase mainly consists of Cr and Fe with a small amount of the Ni and Cu. In contrast, irregular and spherical shaped nanoparticles (marked by 'i' and 'ii' in Fig. 6a) are identified as Ni(Ti)-rich and Cu-rich phases. The precipitation of Ti(Ni)-rich and Cu-rich nanoprecipitates in the CrFe-rich BCC phase is also considered as a result of the high negative ΔH_{mix} value between Ti and Ni and the positive ΔH_{mix} value of Cu with

Fig. 5 TEM-EDS elemental distribution of as-cast $(CrFeNiCu)_{95}Ti_5$ HEA: **a** HAADF image and selected region for elemental mapping; **b–f** corresponding EDS elemental maps of Cr, Fe, Ni, Cu and Ti
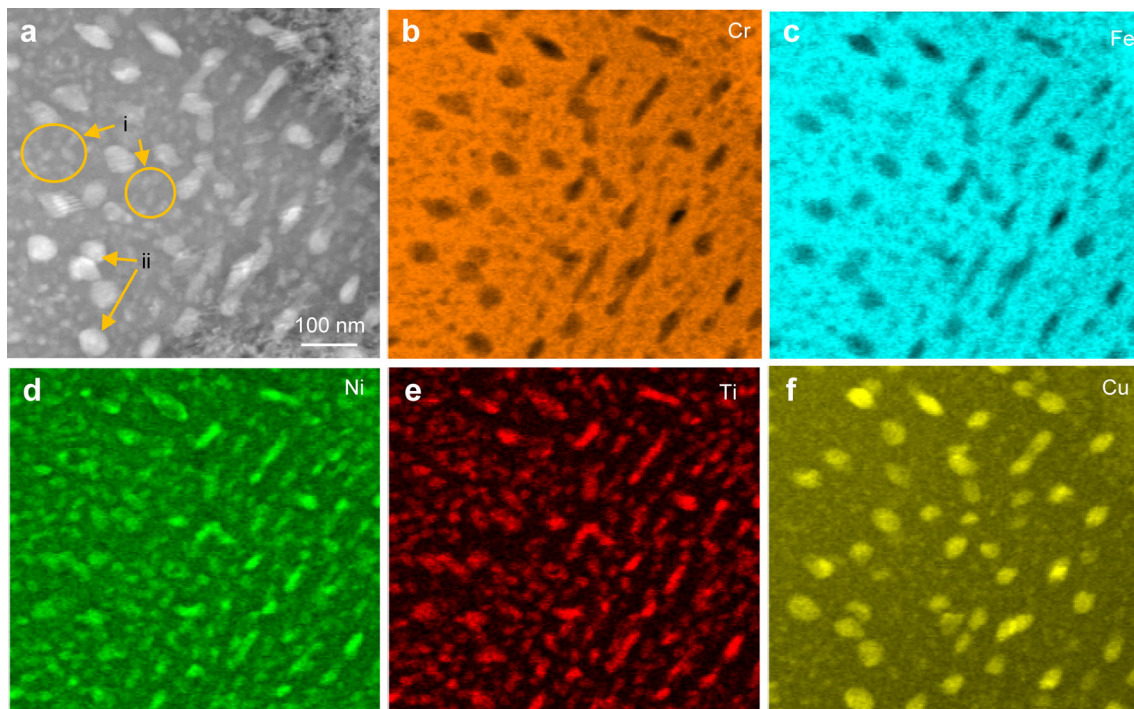
Fig. 6 TEM-EDS elemental distribution of BCC phase in as-cast $(CrFeNiCu)_{95}Ti_5$ HEA: **a** highly magnified HAADF image of BCC phase; **b–f** corresponding elemental maps of Cr, Fe, Ni, Ti and Cu

Cr, Fe and Ni. The addition of Ti and Cu can promote the precipitation of $L1_2$-Ni_3Ti type phase and Cu-rich FCC phase in HEAs; fine $L1_2$-Ni_3Ti type precipitates with the size of 20–100 nm were homogeneously distributed in dendritic regions [42–45]. Based on TEM results in Figs. 4–6, it is concluded that the large negative and positive ΔH_{mix} values of alloying elements result in the solute partitioning or segregation, which induces the nanoprecipitation of $L1_2$ and Cu–rich FCC phases in BCC phase [46–49]. It is well known that nanoprecipitation in BCC phase is effective to enhance the mechanical properties of HEAs [50].

3.3 Mechanical properties

The compressive engineering stress − strain curves of as-cast $(CrFeNiCu)_{100-x}Ti_x$ HEAs and the yield strength and Vickers micro-hardness as a function of volume fraction of BCC phase are shown in Fig. 7a, b. Mechanical characteristics, such as yield strength (σ_y), ultimate strength (σ_{max}), plastic strain (ε_p), and the Vickers micro-hardness values are summarized in Table 3. The yield strength of the as-cast CrFeNiCu HEA with FCC1 and FCC2 phases is 291 MPa and deforms plastically more than 40% without fracture. The yield strength increases from 578 MPa in
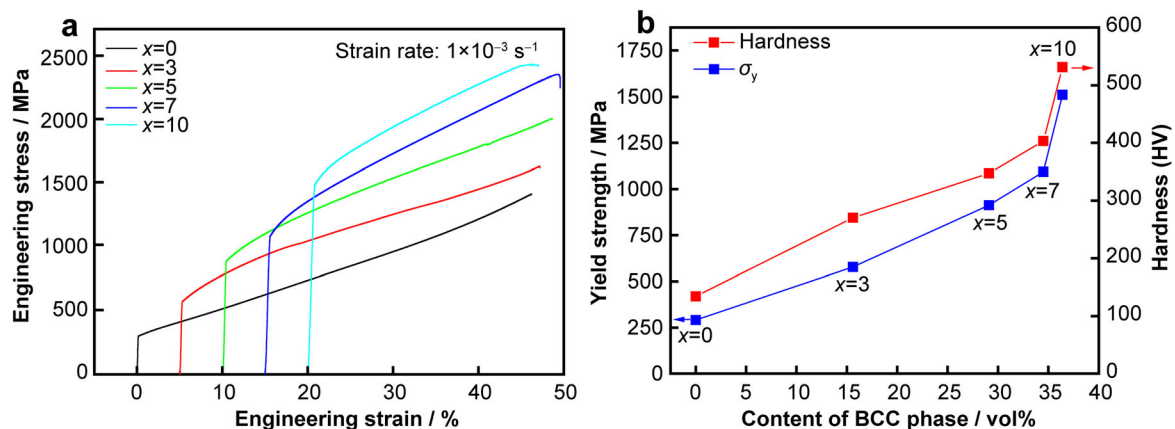
Fig. 7 a Compressive engineering stress−strain curves of as-cast $(CrFeNiCu)_{100-x}Ti_x$ HEAs; **b** yield strength (σ_y) and Vickers hardness values as a function of volume fraction of BCC phase

Table 3 Mechanical properties of as-cast $(CrFeNiCu)_{100-x}Ti_x$ HEAs

Alloys	σ_y / MPa	σ_{max} / MPa	ε_p / %	Hardness (HV)
CrFeNiCu	291	Not fractured	Not fractured	134.3
$(CrFeNiCu)_{97}Ti_3$	578	Not fractured	Not fractured	270.4
$(CrFeNiCu)_{95}Ti_5$	913	Not fractured	Not fractured	347.4
$(CrFeNiCu)_{93}Ti_7$	1094	2358	32.57	403.2
$(CrFeNiCu)_{90}Ti_{10}$	1511	2404	24.09	531.2

$(CrFeNiCu)_{97}Ti_3$ HEA to 1511 MPa in $(CrFeNiCu)_{90}Ti_{10}$ HEA after the addition of Ti. Moreover, the hardness of the alloys is enhanced approximately 4 times (from HV 134.3 to HV 531.2) with the addition of Ti. Figure 7b illustrates the change in yield strength and Vickers hardness as a function of the volume fraction of the BCC phase including a number of nanoparticles. The yield strength and hardness values exhibit almost linear increasing tendency with increasing volume fraction of the BCC phase. Thus, the strength of the as-cast $(CrFeNiCu)_{100-x}Ti_x$ HEAs depends strongly on the volume fraction of BCC phase. However, a high volume fraction of over 34% of BCC phase reduces plasticity. CrFeNiCu, $(CrFeNiCu)_{97}Ti_3$, and $(CrFeNiCu)_{95}Ti_5$ HEAs deform plastically more than 40% without fracture with an increase in the volume fraction of BCC phase to 29%. By contrast, $(CrFeNiCu)_{93}Ti_7$ and $(CrFeNiCu)_{90}Ti_{10}$ HEAs fail during plastic deformation. Nevertheless, $(CrFeNiCu)_{93}Ti_7$ and $(CrFeNiCu)_{90}Ti_{10}$ HEAs show acceptable plasticity of 32.5% and 24.1%, respectively. In conclusion, introduction of BCC phase with nanoprecipitates in CrFeNiCo HEA with FCC1 and FCC2 phases plays an important role to enhance the strength of HEAs with reasonable plasticity.

To understand the detailed deformation behavior of non-fractured and fractured HEAs, the lateral surface of as-deformed $(CrFeNiCu)_{95}Ti_5$ and $(CrFeNiCu)_{90}Ti_{10}$ HEAs is examined by SEM, as shown in Fig. 8a, b. Highly dense

wavy shear bands (marked by yellow-dotted circles) are found in as-deformed $(CrFeNiCu)_{95}Ti_5$ HEA, indicating severe plastic deformation. By contrast, as-deformed $(CrFeNiCu)_{90}Ti_{10}$ HEA exhibits the linear propagation of relatively low dense shear bands along the maximum shear stress direction ($\theta = 45°$ with uniaxial stress). According to the microstructural observation in Fig. 3, it is believed that wavy shear bands in $(CrFeNiCu)_{95}Ti_5$ HEA propagate along the boundary of the spherical FCC1 dendrite which can retard its propagation. Moreover, the strong interaction between shear bands also retards its propagation. On the other hand, $(CrFeNiCu)_{90}Ti_{10}$ HEA containing a high volume fraction of the BCC phase yields at a much higher stress level and is difficult to suppress the propagation of shear bands along the maximum shear stress direction.

According to the investigations in the microstructure and mechanical characteristics of present $(CrFeNiCu)_{100-x}Ti_x$ ($x = 0, 3, 5, 7$ and 10; at%) HEAs, it is concluded that the minor addition of Ti with a large negative ΔH_{mix} value between constituent elements forms CrFe-rich BCC, CrFeNi-rich FFC1 and Cu-rich FCC2 phases. Although VEC value of the alloys is found to be higher than 8, BCC phase is stable and has higher compatibility than FCC1 and FCC2 phases. The formation of BCC phase significantly improves the yield strength of $(CrFeNiCu)_{100-x}Ti_x$ HEAs. Therefore, it is believed that the minor addition of an alloying element by considering the thermophysical parameter (ΔH_{mix}) plays an important role in developing the microstructure with solid solutions, which improves the mechanical properties of HEAs.

4 Conclusion

In this work, the influence of the Ti content on phase formation, microstructure, and mechanical properties of the $(CrFeNiCu)_{100-x}Ti_x$ ($x = 0, 3, 5, 7$ and 10; at%) HEAs was systematically investigated. CrFeNiCu HEA consisted of a dual-phase structure with CrFeNi-rich FCC dendrite and Cu-rich interdendrite phases. The addition of Ti to the
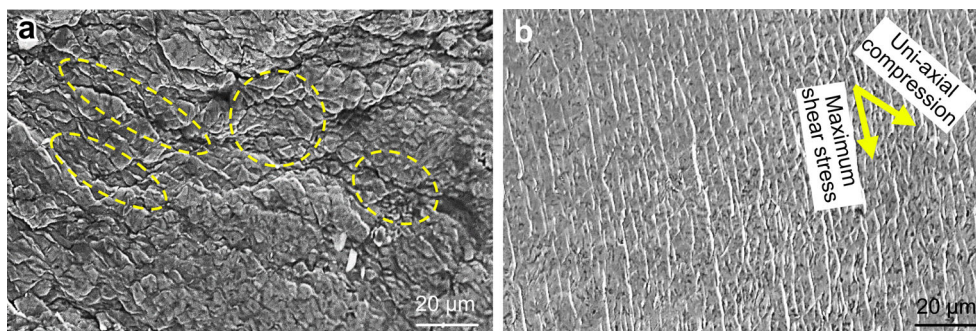
Fig. 8 SEM images of lateral surfaces of as-deformed **a** $(CrFeNiCu)_{95}Ti_5$ and **b** $(CrFeNiCu)_{90}Ti_{10}$ HEAs

(CrFeNiCu)$_{100-x}$Ti$_x$ HEAs led to forming multiple solid solutions: (i) primary CrFe-rich BCC phase, (ii) CrFeNi-rich FCC1 phase, and (iii) Cu-rich FCC2 phase. Ti element was segregated primarily in the CrFeNi-rich FCC phase because of a large negative ΔH_{mix} between Ti and Ni (-35 kJ·mol^{-1}). The relatively low negative ΔH_{mix} value between Ti and Cr (-7 kJ·mol^{-1}) induced the formation of the Cr-rich BCC phase. The volume fraction of the BCC phase gradually increased to 36.5% with the increase in Ti content up to 10 at%, whereas the volume ratio of FCC1 and FCC2 phases was constant ($V_{FCC2}/V_{FCC1} \approx 0.32$). The yield strength and hardness of HEAs were significantly enhanced from 291 to 1511 MPa and HV 134.3 to HV 531.2, respectively, with the Ti content increasing up to 10 at%. Moreover, HEAs with 29 vol% BCC exhibited excellent plastic strain of more than 40% without fracture. However, the plasticity of HEAs was reduced to 24.09% when the volume fraction of the BCC phase increased to 36.5%.

Declarations

Conflict of interests The authors declare that they have no conflict of interest.

References

[1] Yeh JW, Chen SK, Lin SJ, Gan JY, Chin TS, Shun TT, Tsau CH, Chang SY. Nanostructured high-entropy alloys with multiple principal elements: novel alloy design concepts and outcomes. Adv Eng Mater. 2004;6(5):299. https://doi.org/10.1002/adem.200300567.

[2] Lu ZP, Wang H, Chen MW, Baker I, Yeh JW, Liu CT, Nieh TG. An assessment on the future development of high-entropy alloys: summary from a recent workshop. Intermetallics. 2015;66:67. https://doi.org/10.1016/j.intermet.2015.06.021.

[3] Tsai MH, Yeh JW. High-entropy alloys: a critical review. Mater Res Lett. 2014;2(3):107. https://doi.org/10.1080/21663831.2014.912690.

[4] Miracle DB, Senkov ON. A critical review of high entropy alloys and related concepts. Acta Mater. 2017;122:448. https://doi.org/10.1016/j.actamat.2016.08.081.

[5] Yeh JW. Recent progress in high-entropy alloys. Ann Chim Sci Des Mater. 2016;31(6):633. https://doi.org/10.3166/acsm.31.633-648.

[6] Guo S, Liu CT. Phase stability in high entropy alloys: formation of solid-solution phase or amorphous phase. Prog Nat Sci Mater Int. 2011;21(6):433. https://doi.org/10.1016/S1002-0071(12)60080-X.

[7] Huang PK, Yeh JW, Shun TT, Chen SK. Multi-principal-element alloys with improved oxidation and wear resistance for thermal spray coating. Adv Eng Mater. 2004;6(1–2):74. https://doi.org/10.1002/adem.200300507.

[8] Li Z, Pradeep KG, Deng Y, Rabbe D, Tasan CC. Metastable high-entropy dual-phase alloys overcome the strength-ductility trade-off. Nature. 2016;534:227. https://doi.org/10.1038/nature17981.

[9] Yang T, Zhao YL, Tong Y, Jiao ZB, Wei J, Cai JX, Han XD, Chen D, Hu A, Kai JJ, Lu K, Liu Y, Liu CT. Multicomponent intermetallic nanoparticles and superb mechanical behaviors of complex alloys. Science. 2018;362(6417):933. https://doi.org/10.1126/science.aas8815.

[10] Hou J, Zhang M, Yang H, Qiao J, Wu Y. Surface strengthening in Al$_{0.25}$CoCrFeNi high-entropy alloy by boronizing. Mater Lett. 2019;238:258. https://doi.org/10.1016/j.matlet.2018.12.029.

[11] Fan JT, Zhang LJ, Yu PF, Zhang MF, Liu DJ, Zhou Z, Cui P, Ma MZ, Jing Q, Li G, Liu RP. Improved the microstructure and mechanical properties of AlFeCoNi high-entropy alloy by carbon addition. Mater Sci Eng A. 2018;728:30. https://doi.org/10.1016/j.msea.2018.05.013.

[12] Senkov ON, Senkova SV, Dimiduk DM, Woodward C, Miracle DB. Oxidation behavior of a refractory NbCrMo$_{0.5}$Ta$_{0.5}$TiZr alloy. J Mater Sci. 2012;47:6522. https://doi.org/10.1007/s10853-012-6582-0.

[13] Huang YS, Chen L, Lui HW, Cai MH, Yeh JW. Microstructure, hardness, resistivity and thermal stability of sputtered oxide films of AlCoCrCu$_{0.5}$NiFe high-entropy alloy. Mater Sci Eng A. 2007;457:77. https://doi.org/10.1016/j.msea.2006.12.001.

[14] Takeuchi A, Inoue A. Classification of bulk metallic glasses by atomic size difference, heat of mixing and period of constituent elements and its application to characterization of the main alloying element. Mater Trans. 2005;46(12):2817. https://doi.org/10.2320/matertrans.46.2817.

[15] Zhang Y, Zuo TT, Tang Z, Gao MC, Dahmen KA, Liaw PK, Lu ZP. Microstructures and properties of high-entropy alloys. Prog Mater Sci. 2014;61:1. https://doi.org/10.1016/j.pmatsci.2013.10.001.

[16] Yang X, Zhang Y. Prediction of high-entropy stabilized solid-solution in multi-component alloys. Mater Chem Phys. 2012;132(2–3):233. https://doi.org/10.1016/j.matchemphys.2011.11.021.

[17] Guo S, Ng C, Lu J, Liu CT. Effect of valence electron concentration on stability of fcc or bcc phase in high entropy alloys. J Appl Phys. 2011;109(10):103505. https://doi.org/10.1063/1.3587228.

[18] Ng C, Guo S, Luan J, Shi S, Liu CT. Entropy-driven phase stability and slow diffusion kinetics in an Al$_{0.5}$CoCrCuFeNi high entropy alloy. Intermetallics. 2012;31:165. https://doi.org/10.1016/j.intermet.2012.07.001.

[19] He JY, Liu WH, Wang H, Wu Y, Liu XJ, Nieh YG, Lu ZP. Effects of Al addition on structural evolution and tensile properties of the FeCoNiCrMn high-entropy alloy system. Acta Mater. 2014;62:105. https://doi.org/10.1016/j.actamat.2013.09.037.

[20] Liu WH, Lu ZP, He JY, Luan JH, Wang ZJ, Liu B, Liu Y, Chen MW, Liu CT. Ductile CoCrFeNiMo$_x$ high entropy alloys strengthened by hard intermetallic phases. Acta Mater. 2016;116:332. https://doi.org/10.1016/j.actamat.2016.06.063.

[21] Stepanov ND, Shaysultanov DG, Salishchev GA, Tikhonovsky MA, Oleynik EE, Tortika AS, Senkov ON. Effect of V content on microstructure and mechanical properties of the CoCrFeMnNiV$_x$ high entropy alloys. J Alloys Compd. 2015;628:170. https://doi.org/10.1016/j.jallcom.2014.12.157.

[22] Zhu ZG, Ma KH, Wang Q, Shek CH. Compositional dependence of phase formation and mechanical properties in three CoCrFeNi-(Mn/Al/Cu) high entropy alloys. Intermetallcs. 2016;79:1. https://doi.org/10.1016/j.intermet.2016.09.003.

[23] Tung CC, Yeh JW, Shun T, Chen SK, Huang YS, Chen HC. On the elemental effect of AlCoCrCuFeNi high-entropy alloy

system. Mater Lett. 2007;61(1):1. https://doi.org/10.1016/j.matlet.2006.03.140.

[24] Kao YF, Chen SK, Chen TJ, Chu PC, Yeh JW, Lin SJ. Electrical, magnetic, and Hall properties of $Al_x CoCrFeNi$ high-entropy alloys. J Alloys Compd. 2011;509(5):1607. https://doi.org/10.1016/j.jallcom.2010.10.210.

[25] Chen MR, Lin SJ, Yeh JW, Chen SK, Huang YS, Tu CP. Microstructure and properties of $Al_{0.5} CoCrCuFeNiTi_x$ ($x = 0$–2.0) high-entropy alloys. Mater Trans. 2006;47(5):1395. https://doi.org/10.2320/matertrans.47.1395.

[26] Zhou YJ, Zhang Y, Wang YL, Chen GL. Solid solution alloys of $AlCoCrFeNiTi_x$ with excellent room-temperature mechanical properties. Appl Phys Lett. 2007;90(18):181904. https://doi.org/10.1063/1.2734517.

[27] Zhang Y, Zhou YJ, Lin JP, Chen GL, Liaw PK. Solid-solution phase formation rules for multi-component alloys. Adv Eng Mater. 2008;10(6):534. https://doi.org/10.1002/adem.200700240.

[28] Peng Z, Luo ZB, Li BW, Li JF, Luan HW, Gu JL, Wu Y, Yao KF. Microstructure and mechanical properties of lightweight $AlCrTiV_{0.5} Cu_x$ high-entropy alloys. Rare Met. 2022;41(6):2016. https://doi.org/10.1007/s12598-021-01940-9.

[29] Shun TT, Chang LY, Shiu MH. Microstructures and mechanical properties of multiprincipal component $CoCrFeNiTi_x$ alloys. Mater Sci Eng A. 2012;556:170. https://doi.org/10.1016/j.msea.2012.06.075.

[30] Wu H, Huang S, Zhu C, Zhu H, Xie Z. Influence of Cr content on the microstructure and mechanical properties of $Cr_x FeNiCu$ high entropy alloys. Prog Nat Sci Mater Int. 2020;30(2):239. https://doi.org/10.1016/j.pnsc.2020.01.012.

[31] Zhang M, Ma Y, Dong W, Liu X, Lu Y, Zhang Y, Li R, Wang Y, Yu P, Gao Y, Li G. Phase evolution, microstructure, and mechanical behaviors of the $CrFeNiAl_x Ti_y$ medium-entropy alloys. Mater Sci Eng A. 2020;771:138566. https://doi.org/10.1016/j.msea.2019.138566.

[32] Hu Z, Zhan Y, Zhang G, She J, Li C. Effect of rare earth Y addition on the microstructure and mechanical properties of high entropy $AlCoCrCuNiTi$ alloys. Mater Des. 2010;31(3):1599. https://doi.org/10.1016/j.matdes.2009.09.016.

[33] Varalakshmi S, Kamaraj M, Murty BS. Processing and properties of nanocrystalline $CuNiCoZnAlTi$ high entropy alloys by mechanical alloying. Mater Sci Eng A. 2010;527(4–5):1027. https://doi.org/10.1016/j.msea.2009.09.019.

[34] Wang XF, Zhang Y, Qiao Y, Chen GL. Novel microstructure and properties of multicomponent $CoCrCuFeNiTi_x$ alloys. Intermetallics. 2007;15(3):357. https://doi.org/10.1016/j.intermet.2006.08.005.

[35] Yang T, Zhao Y, Liu W, Kai J, Liu C. $L1_2$-strengthened high-entropy alloys for advanced structural application. J Mater Res. 2018;33:2983. https://doi.org/10.1557/jmr.2018.186.

[36] Gwalani B, Choudhuri D, Soni V, Ren Y, Styles M, Hwang JY, Nam SJ, Ryu H, Hong SH, Banerjee R. Cu assisted stabilization and nucleation of L12 precipitates in $Al_{0.3} CuFeCrNi_2$ fcc-based high entropy alloy. Acta Mater. 2017;129:170. https://doi.org/10.1016/j.actamat.2017.02.053.

[37] Borkar T, Gwalani B, Choudhuri D, Mikler CV, Yannetta CJ, Chen X, Ramanujan RV, Styles MJ, Gibson MA Banerjee R. A combinatorial assessment of $Al_x CrCuFeNi_2$ ($0 < x < 15$) complex concentrated alloys: Microstructure, microhardness, and magnetic properties. Acta Mater. 2016. https://doi.org/10.1016/j.actamat.2016.06.025.

[38] Liang YJ, Wang L, Wen Y, Cheng B, Wu Q, Cao T, Xiao Q, Xue Y, Sha G, Wang Y, Ren Y, Li X, Wang L, Wang F, Cai H. High-content ductile coherent nanoprecipitates achieve ultrastrong high-entropy alloys. Nat Commun. 2018;9:4063. https://doi.org/10.1038/s41467-018-06600-8.

[39] Jumaev E, Abbas MA, Mun SC, Song G, Hong SJ, Kim KB. Nano-scale structural evolution of quaternary $AlCrFeNi$ based high entropy alloys by the addition of specific minor elements and its effect on mechanical characteristics. J Alloys Compd. 2021;868:159217. https://doi.org/10.1016/j.jallcom.2021.159217.

[40] Gao S, Kong T, Zhang M, Chen X, Sui YW, Ren YJ, Qi JQ, Wei FX, He YZ, Meng QK, Sun Z. Effects of titanium addition on microstructure and mechanical properties of $CrFeNiTi_x$ ($x = 0.2$–0.6) compositionally complex alloys. J Mater Res. 2019;34:819. https://doi.org/10.1557/jmr.2019.40.

[41] Yang HX, Li JS, Guo T, Wang WY, Kou HC, Wang J. Evolution of microstructure and hardness in a dual-phase $Al_{0.5} CoCrFeNi$ high-entropy alloy with different grain sizes. Rare Met. 2020;39(2):156. https://doi.org/10.1007/s12598-019-01320-4.

[42] Ding J, Xu H, Li X, Liu M, Zhang T. The similarity of elements in multi-principle element alloys based on a new criterion for phase constitution. Mater Des. 2021;207:109849. https://doi.org/10.1016/j.matdes.2021.109849.

[43] Bai X, Fang W, Chang R, Yu H, Zhang X, Yin F. Effect of Al and Ti addition on precipitation behavior and mechanical properties of $Co_{35} Cr_{25} Fe_{40-x} Ni_x$ TRIP high entropy alloys. Mater Sci Eng A. 2019;767:138403. https://doi.org/10.1016/j.msea.2019.138403.

[44] Zhang L, Zhou Y, Jin X, Du X, Li B. Precipitation-hardened high entropy alloys with exellent tensile properties. Mater Sci Eng A. 2018;732:186. https://doi.org/10.1016/j.msea.2018.06.102.

[45] He JY, Wang H, Huang HL, Xu XD, Chen MW, Wu Y, Liu XJ, Nieh TG, An K, Lu ZP. A precipitation-hardened high-entropy alloy with outstanding tensile properties. Acta Mater. 2016;102:187. https://doi.org/10.1016/j.actamat.2015.08.076.

[46] Wang L, Wu X, Su H, Deng B, Liu G, Han Z, Su Y, Huang Y, Zhang Y, Shen J, Zhang G. Microstructure and mechanical property of novel $L1_2$ nanoparticles-strengthened CoFeNi-based medium entropy alloys. Mater Sci Eng A. 2022;840:142917. https://doi.org/10.1016/j.msea.2022.142917.

[47] Tong Y, Chen D, Han B, Wang J, Feng R, Yang T, Zhao C, Zhao YL, Guo W, Shimizu Y, Liu CT, Liaw PK, Inoue K, Nagai Y, Hu A, Kai JJ. Outstanding tensile properties of a precipitation-strengthened $FeCoNiCrTi_{0.2}$ high-entropy alloy at room and cryogenic temperatures. Acta Mater. 2019;165:228. https://doi.org/10.1016/j.actamat.2018.11.049.

[48] Mehranpour MS, Shahmir H, Derakhshandeh A, Nili-Ahmadabadi M. Significance of Ti addition on precipitation in CoCrFeNiMn high-entropy alloy. J Alloys Compd. 2021;888:2. https://doi.org/10.1016/j.jallcom.2021.161530.

[49] Niu M, Zhou G, Wang W, Shahzad MB, Shan Y, Yang K. Precipitate evolution and strengthening behavior during aging process in a 2.5 GPa grade maraging steel. Acta Mater. 2019;179:296. https://doi.org/10.1016/j.actamat.2019.08.042.

[50] Jumaev E, Hong SH, Kim JT, Park HJ, Kim YS, Mun SC, Park JY, Song G, Lee JK, Min BH, Lee T, Kim KB. Chemical evolution-induced strengthening on $AlCoCrNi$ dual-phase high-entropy alloy with high specific strength. J Alloys Compd. 2019;777:828. https://doi.org/10.1016/j.jallcom.2018.11.057.